



## OPEN ACCESS

## EDITED BY

Satoru Yamaguchi,  
National Research Institute for Earth Science  
and Disaster Resilience (NIED), Japan

## REVIEWED BY

Bangjun Cao,  
Chengdu University of Information  
Technology, China  
Yanzhao Zhou,  
Hebei Normal University, China  
Kezhen Chong,

Pacific Northwest National Laboratory (DOE),  
United States

## \*CORRESPONDENCE

Michael Haugeneder,  
✉ michael.haugeneder@slf.ch

RECEIVED 10 April 2024

ACCEPTED 01 October 2024

PUBLISHED 29 October 2024

## CITATION

Haugeneder M, Lehning M, Hames O,  
Jafari M, Reynolds D and Mott R (2024) Large  
eddy simulation of near-surface boundary  
layer dynamics over patchy snow.  
*Front. Earth Sci.* 12:1415327.  
doi: 10.3389/feart.2024.1415327

## COPYRIGHT

© 2024 Haugeneder, Lehning, Hames, Jafari,  
Reynolds and Mott. This is an open-access  
article distributed under the terms of the  
[Creative Commons Attribution License \(CC  
BY\)](https://creativecommons.org/licenses/by/4.0/). The use, distribution or reproduction in  
other forums is permitted, provided the  
original author(s) and the copyright owner(s)  
are credited and that the original publication  
in this journal is cited, in accordance with  
accepted academic practice. No use,  
distribution or reproduction is permitted  
which does not comply with these terms.

# Large eddy simulation of near-surface boundary layer dynamics over patchy snow

Michael Haugeneder<sup>1,2\*</sup>, Michael Lehning<sup>1,2</sup>, Océane Hames<sup>1,2</sup>,  
Mahdi Jafari<sup>1</sup>, Dylan Reynolds<sup>1,2</sup> and Rebecca Mott<sup>1</sup>

<sup>1</sup>Snow and atmosphere, WSL Institute for Snow and Avalanche Research SLF, Davos, Switzerland,  
<sup>2</sup>Laboratory of Cryospheric Sciences, School of Architecture, Civil and Environmental Engineering,  
Ecole Polytechnique Fédérale de Lausanne, Lausanne, Switzerland

The near-surface boundary layer over patchy snow is highly heterogeneous and dynamic. Layers of opposing stability coexist within only a few horizontal meters. Conventional experimental methods to investigate this layer suffer from limitations related to the fixed positions of eddy covariance sensors. To overcome these difficulties, we set up a centimeter-resolution large eddy simulation of flow across an idealised transition from bare ground to snow. We force the simulation with high-frequency eddy covariance data recorded during a field campaign. We show that the model can represent the real flow by comparing it to independent eddy covariance data. However, the simulation underestimates vertical wind speed fluctuations, especially at high frequencies. Sensitivity analyses show that this is influenced by grid resolution and surface roughness representation but not much by subgrid-scale parameterization. Nevertheless, the model can reproduce the experimentally observed plumes of warm air intermittently detaching from bare ground and being advected over snow. This process is highly dynamic, with time scales of only a few seconds. We can show that the growth of a stable internal boundary layer adjacent to the snow surface can be approximated by a power law. With low wind speeds, deeper stable layers develop, while strong wind speeds limit the growth. Even close to the surface, the buoyancy fluxes are heterogeneous and driven by terrain variations, which also induce the frequent decoupling of a thin layer adjacent to the snow surface. Our simulations point the path towards generalizing point-based and aerial measurements to three dimensions.

## KEYWORDS

large eddy simulation, near-surface boundary layer, turbulence, patchy snow, stable internal boundary layer, buoyancy flux

## 1 Introduction

In spring, the snow that has accumulated throughout the winter begins to melt. The resulting run-off plays a crucial role, for example, for the ecosystem (Groffman et al., 2001; Wipf and Rixen, 2010; Wheeler et al., 2016; Rixen et al., 2022), drinking water supply (Sturm et al., 2017; Siirila-Woodburn et al., 2021), or hydropower generation (Stucchi et al., 2019; Magnusson et al., 2020). Furthermore, in combination with precipitation, it can amplify the risk of flooding and associated damages (Sui and Koehler, 2001; Würzer et al., 2016; Li et al., 2019; Mott et al., 2023), underscoring the necessity for a precise understanding and prediction of snowmelt dynamics.

The mountain snow cover is heterogeneous on a wide range of scales shaped by accumulation and ablation processes. Preferential deposition (Lehning et al., 2008), wind-induced snow transport (Föhn and Meister, 1983; Pomeroy and Gray, 1995), and avalanches lead to spatially varying snow depth (Quéno et al., 2023; Reynolds et al., 2024). These spatially irregular accumulation features, together with spatially heterogeneous melt, support the formation of patchy snow covers later in spring. Due to its lower albedo, the bare ground heats up faster than adjacent snow patches. In numerical simulations, studies by Ménard et al. (2014), Letcher and Minder (2017), and Schlögl et al. (2018a) demonstrated the resulting warming feedback for the near-surface atmosphere. The surface temperature of the snow is constrained by its melting temperature of 0°C. Consequently, there is a strong horizontal heat flux divergence between positive heat fluxes above bare ground and negative heat fluxes over snow-covered areas (Mott et al., 2015; Schlögl et al., 2018a).

Local-scale winds, influenced by small-scale surface temperature variations (Johnson et al., 1984) interact with larger-scale circulations such as valley breezes. The valley breeze, in turn, is influenced by an elevation gradient in snow cover: Lower parts of the valley are already snow-free, while higher up, the snow cover is still continuous (Farina and Zardi, 2023). The resulting winds mix the heterogeneously stratified air masses above the patchy snow cover. Warm air from bare ground is advected over snow-covered areas, leading to a strongly stratified layering. Close to the snow surface, a stable internal boundary layer (SIBL) forms (Garratt, 1990). A change in sign of sensible heat fluxes defines its upper boundary. Within the SIBL, negative (downward) fluxes prevail, while above it, positive (upward) fluxes align with the locally unstable stratification. The depth of the SIBL fluctuates rapidly depending on various parameters such as wind speed or stability (Mott et al., 2013; Schlögl et al., 2018a). In a recent experimental study, Haugeneder et al. (2024) examined the growth of a SIBL adjacent to a snow patch over a 3 week period of melt out. They observed that the depth of the SIBL decreased as the snow cover fraction diminished. Additionally, they noted that warm air plumes were intermittently advected over the snow surface, limiting the growth of the SIBL. These intermittent advections occurred on timescales of only a few seconds and only affected the lowest 1 m of the atmosphere adjacent to the snow surface. Thus, the feedback loops between heterogeneous surfaces in spring, the near-surface atmosphere, and the snow-atmosphere interaction processes are highly complex. Further experimental studies are essential for a comprehensive understanding and the development of valid parameterizations for models.

Experimentally investigating the atmosphere close to the surface poses some difficulties. Conventional eddy covariance (EC) measurements are limited to fixed positions and can not be deployed arbitrarily close to the surface (Stiperski and Rotach, 2016). Granger et al. (2006) performed temperature profile measurements at several positions across the transition from bare ground to snow using fine-wire thermocouples. However, this setup can also only sample data at limited locations. Recently, Haugeneder et al. (2023) adapted an approach from Grudzielanek and Cermak (2015) that allows aerial estimations of air temperature and wind speed close to the surface. In this technique, a thermal infrared camera pointing to thin vertically deployed synthetic screens records frames

at 30 Hz. Since the screens have a low heat capacity, their surface temperature can be used as a proxy for the local air temperature. The measurements offer a spatial resolution of 0.5 cm and give insights into the dynamics of the near-surface atmospheric layer. However, they represent only snapshots in time and are confined to small measurement domains. Obtaining a comprehensive understanding of spatial dynamics solely from such measurements is challenging.

High-resolution numerical simulations offer the possibility to bridge the gap between point or aerial measurements and a full three-dimensional representation of the flow across the transition from bare ground to snow. The basis of most fluid dynamics simulations is the Navier-Stokes equations. The coupled system of partial differential equations describes and predicts the three-dimensional momentum field. A common technique to solve the coupled system is the Reynolds-averaged Navier-Stokes (RANS) approach. The Navier-Stokes equations are solved in RANS for time-averaged quantities, and turbulent motions of higher frequencies are parameterized. Due to its computational efficiency, it is used for modeling studies of the ABL (e.g., Balogh et al., 2012; Hames et al., 2022). It has also been used to study atmosphere-cryosphere interactions (Hames et al., 2022; Jafari et al., 2022). Challenges arise when the focus of the research is on turbulent quantities. Naturally, turbulence is not steady-state but transient. Therefore, only looking at time-averaged quantities does not yield enough information.

On the opposite side of the complexity spectrum for solving fluid dynamics problems is direct numerical simulation (DNS) (Pope, 2000). The Navier-Stokes equations can be accurately solved in idealized scenarios with relatively moderate Reynolds numbers. Eddies of all scales are directly resolved, and therefore no turbulence parameterization is necessary. For example, van der Valk et al. (2022) use a DNS model to simulate the near-surface boundary layer over patchy snow. Using temperature profile measurements above patchy snow from Harder et al. (2017), they found spatial variability in sensible heat fluxes that result in spatially heterogeneous melt rates. However, this computationally costly approach is limited to highly idealized conditions.

Large Eddy Simulations (LES) act as a robust intermediary, filling the complexity gap between RANS and DNS. By spatially filtering the Navier-Stokes equations, LES directly represents supra-filter scale motions while parameterizing sub-filter motions (Pope, 2000). Relevant energy-containing scales are directly resolved by choosing a suitable filter scale. In recent decades, multiple studies have applied the LES approach to study ABLs of various stability on a wide range of scales. Some more recent studies include Huang and Bou-Zeid (2013); Richardson et al. (2013); Zwaafink et al. (2014); Smith and Porté-Agel (2014); Sigmund et al. (2022); Melo et al. (2024); Zahn and Bou-Zeid (2024). The review of Stoll et al. (2020) provides a comprehensive overview of studies.

In this work, we set up, validate, and analyze an LES simulation to study the near-surface atmosphere adjacent to the transition from bare ground to snow. Ultimately, we aim to generalize data recorded during a previous field campaign to get more information on the fetch dependence of heat fluxes close to the surface. Therefore, Sect. 2 gives an overview of the experimental data and the setup of the model followed by a validation of the model results with measurements in Sect. 3. In Sect. 4 we use the simulation results to investigate the near-surface boundary layer dynamics. Specifically, we examine the intermittent advection of plumes of warm air over

the snow and the spatial and temporal dynamics of the SIBL. Furthermore, in Sect. 4.3 we analyze the dependence of vertical profiles of temperature and wind speed, as well as the SIBL depth, on wind speed. Section 5 summarizes the findings and gives a brief outlook.

## 2 Methods

### 2.1 Study site

In late spring 2021, we collected data during a comprehensive field campaign in the Dischma valley near Davos (Switzerland). The valley axis of the straight high alpine valley is oriented in the southeast-northwest direction. Steep slopes enclose the valley floor with an elevation difference of approximately 1000 m. The area has been extensively studied (Urfer-Henneberger, 1970; Lehning et al., 2006; Bavay et al., 2009; Brauchli et al., 2017; Wever et al., 2017; Mott et al., 2017; Schlögl et al., 2018a; b; Gerber et al., 2019; Carletti et al., 2022; Reynolds et al., 2023). Dürrboden, the flat measurement site at an elevation of 2010 m a.g.l., is located at the end of the valley. The map in Figure 1 gives an overview of the area. The right part of Figure 1 shows an aerial overview picture captured on 30 May 2021 by an Uncrewed Aerial Vehicle (UAV). Bare patches have already emerged.

To force and validate the LES simulation presented in this study, we use eddy covariance (EC) data recorded during this campaign. We deployed multiple sensors at various locations and heights. We installed two IRGASONS (Campbell Scientific, Logan, Utah, United States) on ECT1 at 1.2 m above the surface and on ECT2 at 0.9 m above the surface. Furthermore, at ECT2, we installed two CSAT3Bs (Campbell Scientific, Logan, Utah, United States) at heights of 1.9 and 2.9 m, together with a Campbell PT1000 ventilated air temperature sensor (Campbell Scientific, Logan, Utah, United States) positioned at 1 m above the surface. All EC sensors recorded data at a sampling frequency of 20 Hz. The lines in the UAV image indicate the 80% flux footprints as described by the parameterization of Kljun et al. (2015). For interpretation, we note that the LES simulation is forced with data taken on 31 May 2021, so 1 day after the UAV image in Figure 1 was taken. During this period of snow melt, bare patches emerge and extend rapidly. For the snow cover on 31 May, the area within the flux footprints of both ECTs was mostly snow-covered. The automatic weather station (AWS) was installed  $\approx 30$  m upwind of the ECTs. In the present study, we use air temperature measured at the height of 3.7 m above the surface by a HygroVue 5 (Campbell Scientific, Logan, Utah, United States). The AWS recorded data averaged every 10 min.

In addition to conventional EC measurements, we deployed thin synthetic screens vertically positioned across the transition from bare ground to snow. Using a thermal infrared camera to film these screens, we obtained surface temperatures at a spatial resolution of 0.6 cm and a temporal resolution of 30 Hz. The screens are thin enough to quickly adjust to the ambient air temperature. Therefore, the recorded surface temperature of the screens serves as a proxy for the local air temperature. The data visualizes the temperature stratification and its dynamics adjacent to the surface. In the following, we will refer to this setup as the IR setup. We refer

the reader to Haugeneder et al. (2023) for further details about the field campaign.

### 2.2 Large eddy simulation

This study aims to set up, validate, and analyze a high-resolution numerical simulation of atmospheric flow over a single bare ground to snow transition forced with measurement data collected as described above. Therefore, we employ a large-eddy simulation (LES). LESs were first introduced in 1963 by Smagorinski (1963). Since then, the approach has grown rapidly and has become a popular and powerful tool to investigate atmospheric processes on various scales (Stoll et al., 2020).

In the following, we quickly summarize the basic concept and equations, which are important for the interpretation of the later results. For easier notation, we use the Einstein summation convention, in which a summation over the three spatial directions  $x$ ,  $y$ , and  $z$  is implied for repeated indices. As an example, we show the momentum equation.

The Navier-Stokes equations for incompressible flow predict the three-component velocity field  $u_i$  at time  $t$ .

$$\frac{\partial u_i}{\partial t} + u_j \frac{\partial}{\partial x_j} u_i = \nu \frac{\partial^2 u_i}{\partial x_j \partial x_j} - \frac{1}{\rho} \frac{\partial p}{\partial x_i}. \quad (1)$$

$\nu$  describes the kinematic viscosity,  $\rho$  the fluid density and  $p$  the pressure including gravitational pressure (Pope, 2000). For simplicity, we drop the buoyancy term, which can be written in the Boussinesq approximation as  $-\delta_{iz} g \alpha \Delta T$ , where  $g$  denotes the gravitational acceleration (in the downward  $z$ -direction),  $\alpha$  the thermal expansion coefficient, and  $\Delta T = T - T_0$  the difference between the local temperature and a reference temperature. The additional variable  $T$  can be solved by utilizing energy conservation.

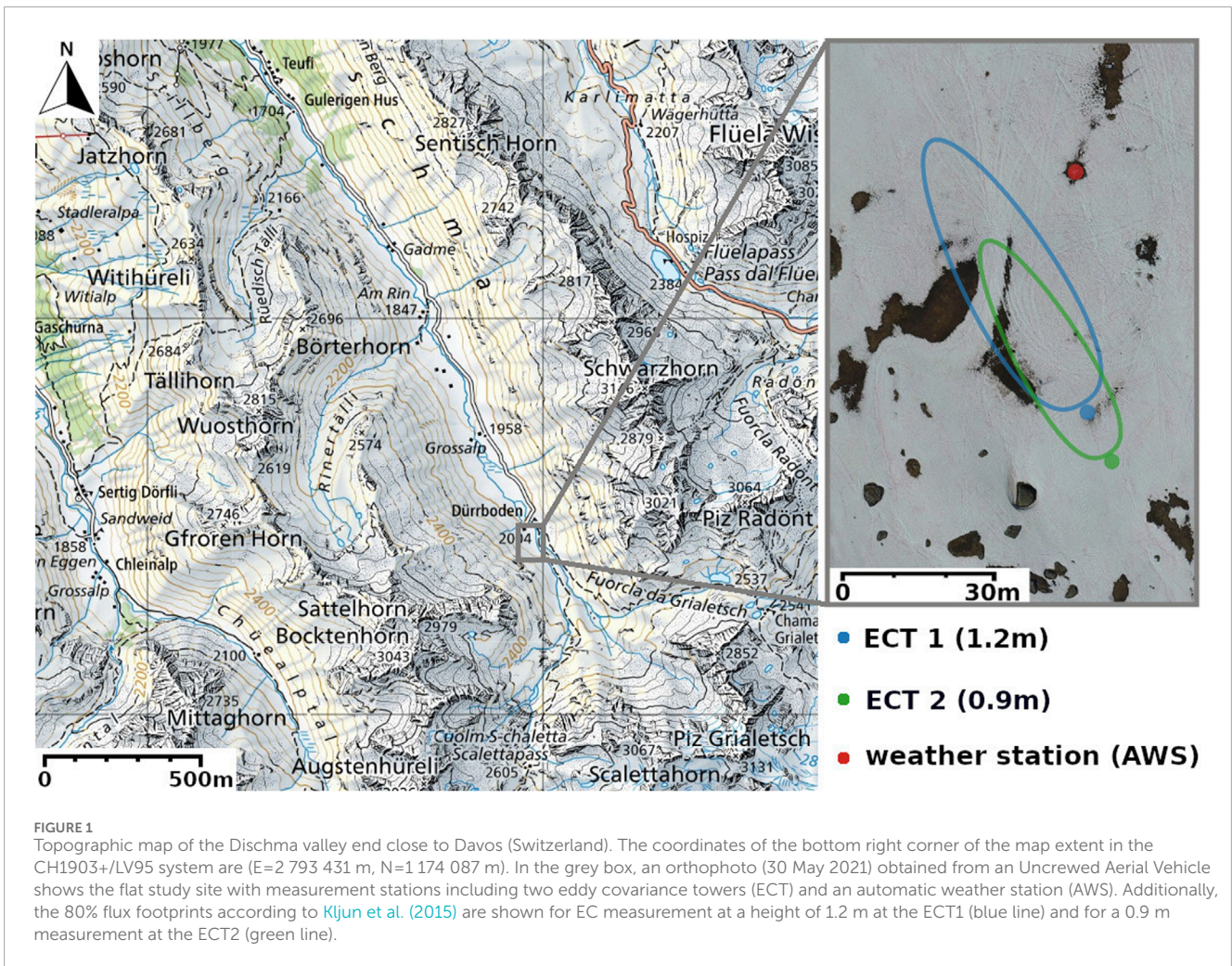
Directly solving Equation 1 and the incompressible continuity equation

$$\frac{\partial u_i}{\partial x_i} = 0$$

is known as Direct Numerical Simulation (DNS). Due to the tremendous computational costs, this is (to date) only possible for highly idealized conditions. To reduce the computational demands, Equation 1 can be filtered. The filter, which can take on various shapes such as spectral cut-off or Gaussian, separates resolved large-scale motions from non-resolved and thus parameterized subgrid-scale (SGS) motions. This filtering step is the cornerstone of LES modelling. In our case, filtering is achieved implicitly by discretizing the mesh (Lund, 2003). We give a more detailed description of the model setup in Sect. 2.3. The filtered Equation 1 are

$$\frac{\partial \overline{u}_i}{\partial t} + \frac{\partial \overline{u}_i \overline{u}_j}{\partial x_j} = \nu \frac{\partial^2 \overline{u}_i}{\partial x_j \partial x_j} - \frac{1}{\rho} \frac{\partial \overline{p}}{\partial x_i}, \quad (2)$$

where variables with an overbar denote filtered quantities. The second term presents a challenge:  $\overline{u}_i \overline{u}_j$  is the filtered product of two unfiltered quantities  $u_i$  and  $u_j$ . This means that to solve Equation 2, knowledge about unfiltered quantities is necessary. This problem is solved by parameterizing the anisotropic residual stress tensor  $\tau_{ij}^r = \tau_{ij}^R - \frac{1}{3} \tau_{ii}^R \delta_{ij}$  where the residual stress tensor is given by  $\tau_{ij}^R =$



$\overline{u_i u_j} - \overline{u_i} \cdot \overline{u_j}$  (Pope, 2000). Multiple approaches with different levels of complexity are available for this SGS parameterization. Despite more sophisticated parameterizations having been suggested (e.g., dynamic SGS model (Germano et al., 1991), Lagrangian dynamic model (Meneveau et al., 1996), or SGS models solving a transport equation (Deardorff, 1974)), we use the computationally efficient Smagorinski-Lilly SGS model (Smagorinski, 1963). From sensitivity analysis we found no strong change in the results when we used, for example, a dynamic Lagrangian SGS model.

The Smagorinski-Lilly SGS model utilizes the concept of viscosity and builds upon the presence of an inertial subrange (Stoll et al., 2020). Within the frequency range of the inertial subrange, turbulent energy is transferred, in the mean, only from larger to smaller scales (Kolmogorov, 1941). If the filter is chosen to be in the inertial subrange, Smagorinski (1963) hypothesize a linear relation between the anisotropic residual stress and the filtered rate of strain  $\overline{S_{ij}}$

$$\tau_{ij}^r = -\nu_r \left( \frac{\partial \overline{u_i}}{\partial x_j} + \frac{\partial \overline{u_j}}{\partial x_i} \right) = -2\nu_r \overline{S_{ij}},$$

where

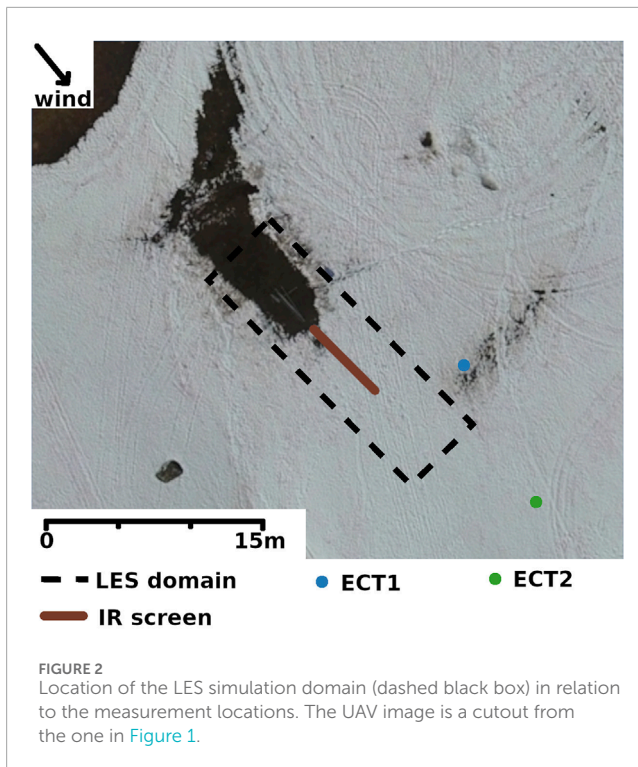
$$\nu_r = (C_s \Delta)^2 \sqrt{2\overline{S_{ij} S_{ij}}}$$

describes the eddy viscosity,  $C_s$  the Smagorinski coefficient and  $\Delta = (\Delta_x \Delta_y \Delta_z)^{\frac{1}{3}}$  the filter width. A disadvantage of the Smagorinski-Lilly SGS model is that it is purely dissipative and not representing the true equilibrium between forward and backward scatter (Stoll et al., 2020). Backward scattering, i.e., the influence of non-resolved subgrid-scale motion on resolved scales, can significantly modify the flow field (Leslie and Quarini, 1979).

### 2.3 Model setup and forcing

We set up the LES simulation across an idealized transition from bare ground to snow. The computational domain spans 20 m along the flow direction ( $x$ ), 6 m in across-flow direction ( $y$ ) and is 5 m high ( $h$ ). We use a horizontal cell width of  $\Delta x = \Delta y = 0.04$  m with a vertical cell height of  $\Delta h = 0.03$  m – 0.07 m. The smallest cells are at the bottom of the domain. With these cell sizes, the simulation includes about  $7.7 \times 10^6$  cells. We use adaptive time-stepping to prevent excess Courant numbers that could cause numerical instability (Moukalled et al., 2016). Throughout the simulation, the median time step is  $\overline{\Delta t} = 8 \times 10^{-3}$  s.

To allow for forcing with high-frequency EC measurements, we use inflow-outflow boundary conditions in the  $x$  direction and cyclic



boundaries in the  $y$  direction. We apply a zero-gradient Neumann boundary condition for momentum and temperature as an upper boundary condition.

The transition between bare ground and snow in the model at  $x = 8$  m is characterized by a change in surface roughness and surface temperature. There were many old footsteps on the snow surface. We estimated the height of the roughness elements on snow from field observations to be  $\approx 0.1$  m. We assumed a height of the roughness elements of  $\approx 0.05$  m for grass. For generating rough surfaces, we use the open-source Python library `tamaas` (available from <https://gitlab.com/tamaas/tamaas/-/tree/master>). It generates random rough surfaces by back-transformation of a given spectrum. To account for the different structures of the surfaces, we not only changed the height of the roughness elements, but also the frequencies contained in the spectrum. For grass, we included higher frequencies to represent finer structures. We set the surface temperature of the snow to the melting point at  $0^\circ\text{C}$ . Using data collected from the thermal infrared camera, we approximated the temperature of the bare ground at  $15^\circ\text{C}$ .

We force the simulation directly with high-frequency EC measurements. To our knowledge, this has not yet been done in such a setup. Figure 2 gives an overview of the domain in relation to the available EC sensors. We chose the location of the domain such that the flow resembles the data captured by the IR screen setup. The idea is to apply the larger scale forcing via measured wind speeds and air temperatures and let the model simulate the surface-driven buoyancy effects at the transition from bare ground to snow.

For wind speed forcing, we fit a logarithmic wind profile (log profile) through the median of 5 min EC data from three sensors at ECT2, which is the only location featuring multiple EC sensors at different heights. In the measurements, we do not see much

difference between wind speed data recorded at ECT1 and ECT2 (apart from a time lag). Therefore, we assume that data from ECT2 sufficiently describes the flow structure at the inflow. To obtain a high-frequency wind profile, we scaled the log profile to the data measured at 0.9 m above the surface at ECT2.

A challenging task in LES modelling is to obtain realistic turbulence at the inlet. We use the divergence-free synthetic eddy method (DFSEM) developed by Poletto et al. (2013). The method generates realistically shaped eddies according to a given mean wind speed, Reynolds stress tensor, and turbulence integral length scale. We use 20 Hz horizontal wind speed data and calculated the Reynolds stress tensor from the 0.9 m EC sensor at ECT2. We also estimate the turbulence length scale from an auto-correlation analysis of this data. Additionally, we assume that the Reynolds stress tensor and the turbulence length scale are constant in the horizontal and vertical directions.

We do not apply vertical wind speed forcing, since we do not have enough measurement data to realistically interpolate, accounting for larger-scale vertical motions. However, the turbulent part of the vertical wind speed is generated by the DFSEM.

For temperature forcing, we use the upwind measurement at the AWS at 3.7 m height (see Figure 1). Since the AWS recorded data only every 10 min, we use the 5 s variations recorded by the ventilated thermometer at ECT2 scaled to the mean temperature measured at the AWS. We then logarithmically scale the air temperature to the surface temperature of bare ground of  $15^\circ\text{C}$  (Högström, 1996).

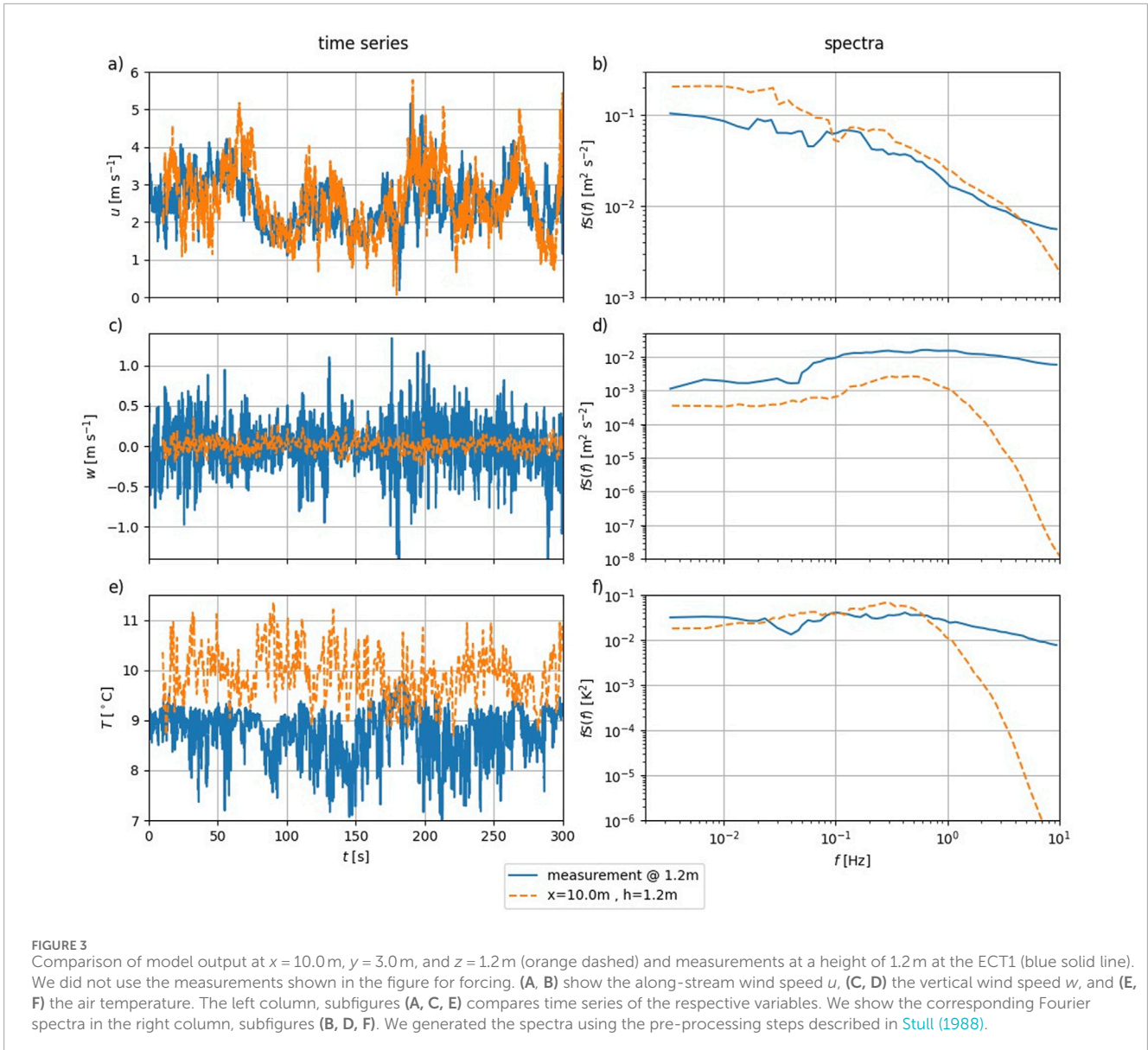
For the analysis in this study, we extract data on a slice aligned with the wind direction at  $y = 3$  m. Furthermore, to account for the spin-up of the simulation, we discard the first 10 s of data.

For the simulation, we use the buoyantBoussinesqPimpleFoam solver (OpenFoam API Guide, 2024) available from the open-source fluid dynamics platform OpenFOAM (Weller et al., 1998). The transient solver is designed for incompressible flow. OpenFOAM uses a finite volume method for discretization.

### 3 Validation of model results against measurements

In this section, our objective is to compare the LES simulation results with eddy covariance (EC) measurements. Therefore, we use the EC measurement at 1.2 m height on the ECT1. This particular EC measurement, not included in the initial model forcing, serves as an independent means of validation. Extracting data from the simulation domain at  $x = 10.0$  m,  $y = 3.0$  m, and  $z = 1.2$  m ensures a sufficient downwind distance to the transition from bare ground to snow. However, when interpreting the results, the reader should keep in mind that the flux footprint of the 1.2 m measurement on the ECT1 (cf. Figure 1) hardly contains any bare ground. Figure 3 compares the LES simulation with the EC measurement. We discard the first 10 s of the simulation results for flow spin up.

The time series of wind speed along the flow presented in Figure 3 agree very well in both the absolute magnitude and the magnitude of the fluctuations. Nevertheless, a slight lag is observed between the two time series. This lag can be attributed to the setup depicted in Figure 1. Data for driving the LES simulations originate from ECT2, whereas the comparison data are obtained from ECT1



approximately 10 m upwind of ECT2. Consequently, the simulation exhibits a lag relative to the measurements. Nonetheless, the good agreement between measurement and simulation is also reflected by the spectra in Figure 3B. Both measurement and simulation agree well on all time scales. Time series and spectra indicate that the LES simulation features a realistic along-stream wind speed.

Furthermore, the mean vertical wind speed of the LES simulation at the extracted point  $\overline{w_{LES}} = 0.011\text{ m s}^{-1}$  is in good agreement with the double-rotated measurement data (and thus  $\overline{w_{EC}} \approx 0\text{ m s}^{-1}$ ). Nevertheless, the simulation underestimates the magnitude of the fluctuations. While EC measurements yield a variance of  $\sigma_{w,EC}^2 = 7.9 \times 10^{-2}\text{ m}^2\text{ s}^{-2}$ , the simulation shows a variance of  $\sigma_{w,LES}^2 = 7.0 \times 10^{-3}\text{ m}^2\text{ s}^{-2}$ . Both variances differ by a factor of 11. This mismatch in the magnitude of the fluctuations is evident from the spectrum depicted in Figure 3D. The simulation notably lacks spectral energy density across all frequencies, with the discrepancy becoming more pronounced for  $f > 1\text{ Hz}$ . Sensitivity

analysis unveiled multiple potential factors contributing to this discrepancy, some of which are interrelated. Specifically, the analysis suggests that grid spacing is critical in accurately representing vertical wind speeds. Conversely, the impact of employing a more sophisticated Sub-Grid-Scale (SGS) model, such as a dynamic Lagrangian SGS model, was relatively small. The gap for high-frequency data and the dependence on the grid spacing indicates that relevant eddy sizes in this strongly heterogeneous setting might even be smaller than the chosen grid spacing of 4 cm (horizontal) and 3 cm–7 cm (vertical). We think there are multiple reasons for these not-captured small-scale eddies. One such factor is the presence of sharp terrain features that remain unresolved by the simulation. In addressing this issue, it was important to add resolved surface roughness. Surface roughness proved crucial, demonstrating a comparable impact to increasing grid resolution (not shown). Furthermore, the model does not account for small-scale heterogeneities in the surface temperature of bare ground

driving smaller-scale (and thus higher frequency) buoyant motion. Another contributing factor could be an inadequate description of inflow conditions. The model is forced by a logarithmic wind profile scaled by a single measurement, which may not adequately capture disturbances in the inflow, such as low-level jets. Finally, the dimensions of the model domain itself influence the flow by constraining the scale of motions within the simulation. Our sensitivity analysis indicates that state-of-the-art SGS models struggle to parameterize these intricate effects. Future work should prioritize efforts to address and improve upon these limitations. However, it is important to note that for our present study, further reduction of grid spacing was unfeasible due to constraints imposed by limited computational resources.

For the comparison of air temperature in [Figure 3E](#), we corrected the measured sonic temperature with the simultaneously measured humidity according to [Schotanus et al. \(1983\)](#). The spectra presented in [Figure 3F](#) indicate a similar mismatch between the EC measurement and the simulation for  $f > 1$  Hz. However, for lower frequencies, both spectra match well. This is also reflected by the time series shown in [Figure 3E](#). The magnitude of the fluctuations seems very similar to the EC data. Not visible from the spectrum, there is a positive temperature bias of  $\approx 1^\circ\text{C}$  of the air temperature extracted from the simulation. Different footprints can explain this bias. The mean temperature used for forcing was recorded at the height of 3.7 m at the AWS (cf. [Figure 1](#)). In contrast, the data shown as the blue curve in [Figure 3E](#) was measured at ECT1.

In summary, the LES simulation demonstrates remarkable capability in replicating the observed horizontal wind speed pattern as measured by a high-frequency EC sensor. Moreover, the mean vertical wind speed and the air temperature fluctuations agree well with the measurements. However, for frequencies exceeding  $f > 1$  Hz, the simulation tends to underestimate the spectral energy densities for  $w$  and  $T$ . We explain this discrepancy with the strongly heterogeneous nature of the setting, which can not be fully represented in fine detail by the model. Despite this limitation, we maintain that the LES simulation yields realistic results suitable for subsequent, semi-quantitative analyses.

## 4 Characterization of near-surface boundary layer dynamics

### 4.1 Intermittent advection

In the following section, we aim to compare the LES simulation results with data obtained from the IR screen setup as described in [Haugeneder et al. \(2023\)](#). Our objective is to demonstrate the model's capability to resolve the dynamics of the near-surface boundary layer accurately. In [Haugeneder et al. \(2024\)](#), the authors describe the intermittent advection of warm air plumes from bare ground over snow, a phenomenon successfully captured using the IR screen setup. We extracted a two-dimensional slice perpendicular to the cross-flow direction from the simulation data to facilitate comparison with our simulations. This slice then shows an aerial overview of the near-surface boundary layer similar to the IR screen data.

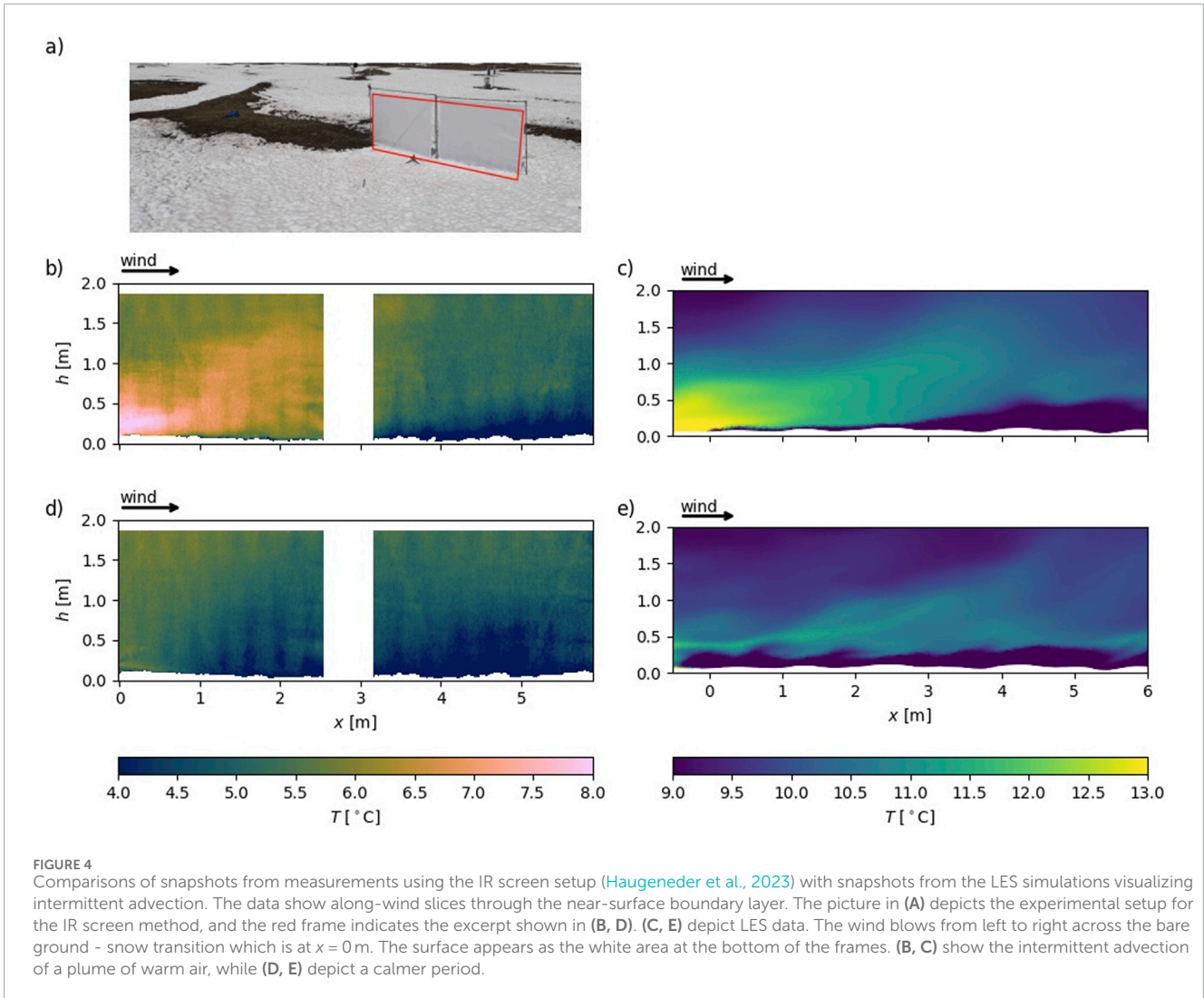
We compare snapshots from the IR screen data ([Figures 4B, D](#)) with snapshots from the slice of the LES simulation ([Figures 4C, E](#))

in [Figure 4](#). Furthermore, the video in the [Supplementary Material](#) visualizes the temporal dynamics. For a better understanding of the processes discussed in the following, we strongly encourage the reader to watch it. In the second row, [Figures 4B, C](#), we show a snapshot taken when a plume of warm air was advected over the snow patch. In both, measurement and simulation data, the air temperature is the highest directly adjacent to the bare surface. The plume of warm air reaches up to  $\approx 1$  m above the surface at  $x = 0$  m. In the measurement, the warm air reaches a few meters along the wind direction over the snow surface. For  $x > 1$  m we detected a shallow layer of cold air close to the snow surface. Further down wind, this layer grows up to 0.5 m depth. The slice of the LES simulation shows a very similar pattern: The plume of warm air reaches  $x \approx 2$  m. Similar to the measurement, a layer of cold air is adjacent to the snow surface. The layer seems to be slightly thicker than the measurement for fetch distances  $x < 2$  m. At  $x = 3$  m it grows as observed from the IR screen measurements. The plume of warm air displaces the cold air layer from left to right.

In the simulation, the layer of cold air adjacent to the snow surface appears to be more clearly separated from the air above. This is especially obvious from the videos in the [Supplementary Material](#). You can see that in the simulation, the wind influences the growth of this layer. However, especially at the leading edge of the snow patch, the depth does not change as much over time as expected from the measurements. This could be explained by vertical wind speeds that are too low and, thus, insufficient vertical mixing. We found from previous simulation runs that the vertical wind speed is an important factor in determining the thickness of the cold air layer in the simulation results. With an underestimated vertical wind speed, there is insufficient vertical mixing to develop a deeper layer of cold air. With a finer grid, we could increase the vertical wind speeds near the surface. However, the fluctuations are still too low as the reader can also see from the comparison in [Figure 3C](#) at 1.2 m above the surface.

Just a few seconds after the advection of the warm air plume, the boundary layer near the surface was distinctly colder, as shown in [Figures 4D, E](#). In the measurement, the layer of cold air adjacent to the snow surface was deeper. Air is significantly colder than in [Figure 4C](#), but some slightly warmer plumes as remnants of a previously advected plume detached from the surface, are visible. A deeper layer of decoupled cold air adjacent to the snow surface develops at the leading edge of the snow patch during more quiescent conditions. The cold air even spreads over bare ground because rising buoyant plumes further to the left lead to a local back-flow close to the surface, sucking in cold air from over the snow. The short time difference between the respective two snapshots emphasizes the strong temporal heterogeneity of the near-surface boundary layer apparent in both the simulation results and the measurements.

The offset in absolute temperature between the measurement and the simulation can be explained by the temperature forcing. Using air temperatures measured at 3.7 m above the surface at the AWS (see [Figure 1](#)), we do not expect a perfect match. The focus is more on the temporal heterogeneity caused by local surface-driven buoyancy effects. Based on the comparison of time series and spectra between measurement and results, [Figure 4](#) demonstrates that our LES model setup is capable of resolving the measured pattern in the dynamics of the near-surface boundary layer above the transition



from bare ground to snow. Furthermore, the above comparison shows the value of visualization using the IR screen setup.

### 4.2 Buoyancy fluxes and stable internal boundary layer growth

By employing EC sensors in the field, we can gather a temporal sequence of data at specific locations. However, it is difficult or even impossible to interpolate or extrapolate the data to regions without sensors spatially. Especially very close to the surface, within the lowest tens of centimeters, most traditional EC sensors do not yield reliable results. Therefore, the data obtained from the validated LES simulation presented in this study is a powerful tool for investigating spatial properties of the near-surface boundary layer. In the following, we investigate the spatial pattern of median buoyancy flux and the growth of the SIBL adjacent to the snow surface downwind of the transition from bare ground to snow.

We therefore calculate the buoyancy fluxes at every grid point of the along-wind slice taken out of the LES simulation. Figure 5A

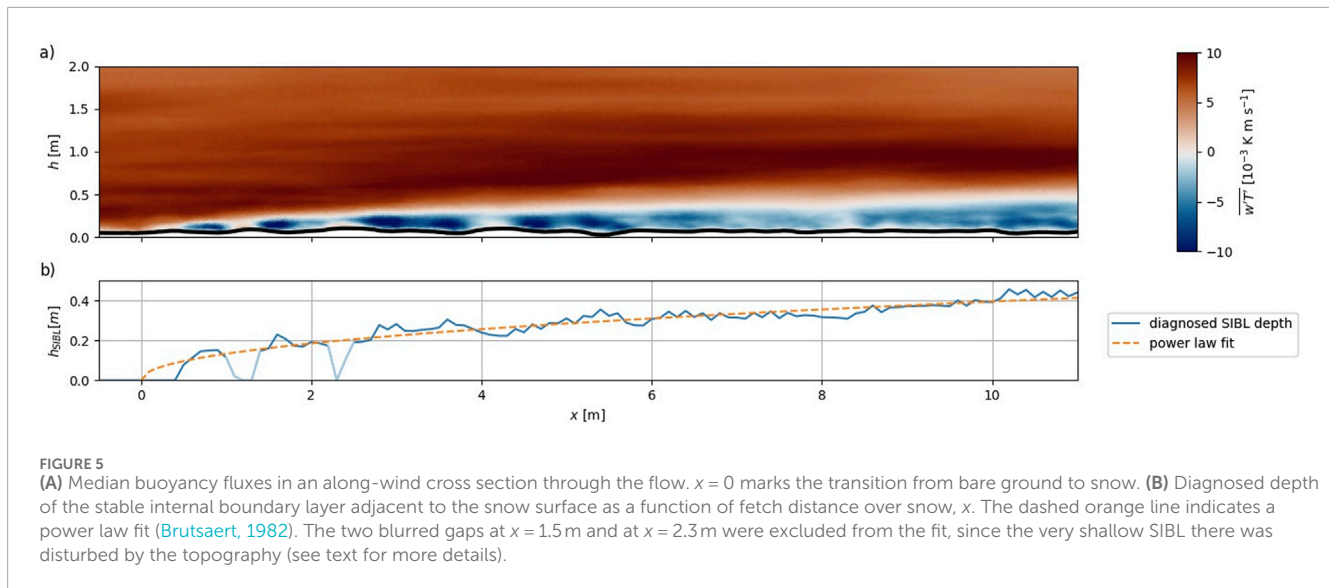
shows the spatial pattern. For the interpretation, the reader should keep in mind that the simulation tends to underestimate vertical wind speeds and, thus, also buoyancy fluxes. The emphasis is here on spatial patterns without claiming full quantitative accuracy. For a median SIBL depth, we take the median of the buoyancy fluxes time series at every grid point. We define the upper boundary of the SIBL by the sign change of the buoyancy fluxes. Within the SIBL, negative (downward) fluxes prevail. While above the SIBL the stratification in our setting is unstable in accordance with positive (upward) fluxes. Figure 5B depicts the diagnosed SIBL depth as a function of fetch distance over snow,  $x$ . As a fit, we apply the commonly used power law (Brutsaert, 1982)

$$h_{SIBL} = c \left( \frac{x}{1 \text{ m}} \right)^b.$$

We exclude the two drops in the diagnosed SIBL height around  $x = 1.2$  m and  $x = 2.3$  m because at these positions, the shallow SIBL is disturbed by the local topography. We discuss this effect in the following passage. The parameters obtained from the least squares fit are.

$$b = 0.47$$





$$c = 0.13 \text{ m.}$$

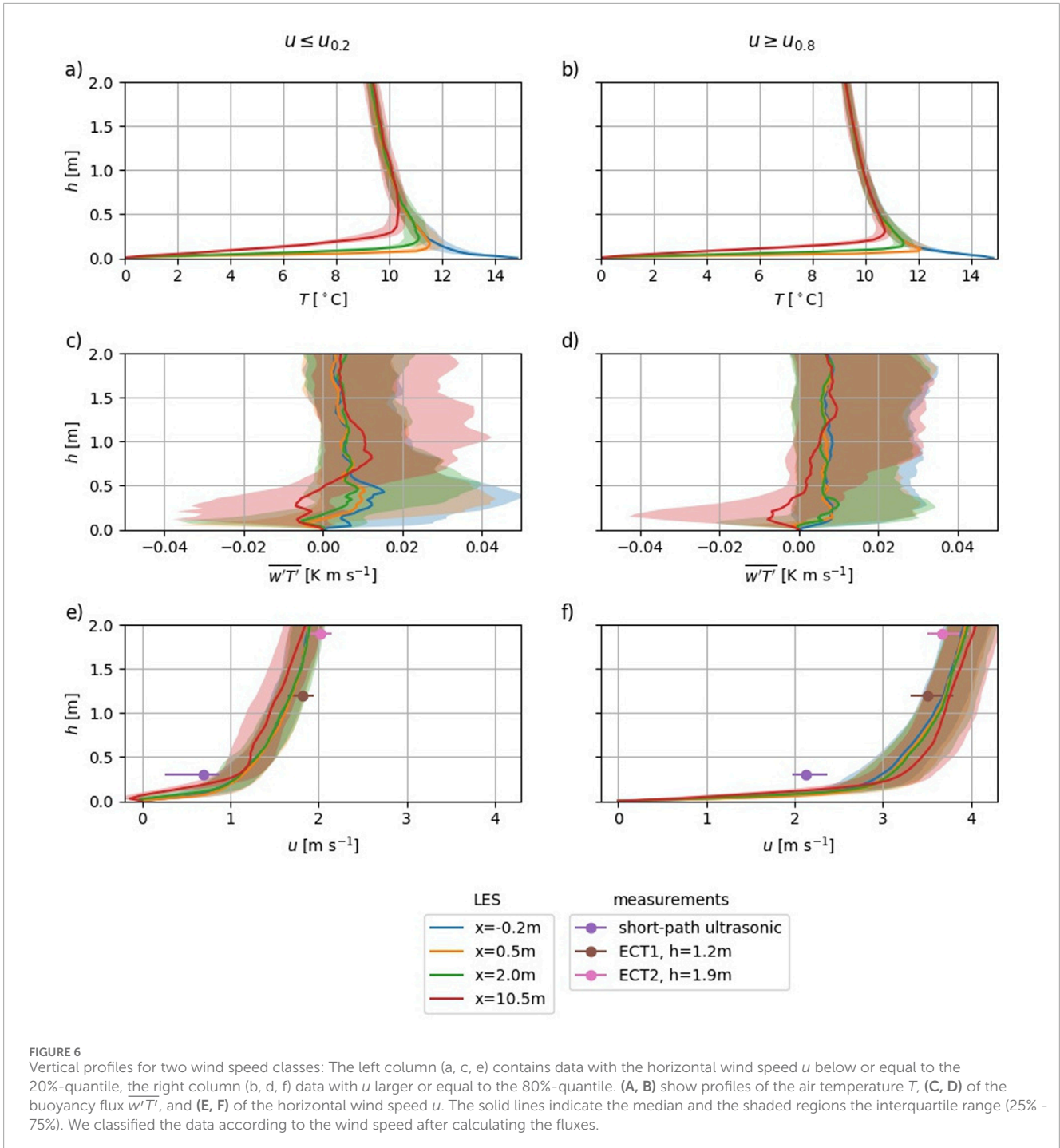
Two different regimes immediately become obvious from Figure 5A. Negative (downward) buoyancy fluxes prevail close to the snow surface. In contrast, the rest of the domain exclusively exhibits positive fluxes. The air heats up over bare ground and is then intermittently advected over the snow surface. Along the trajectory of the plumes, we detect the maximum positive buoyancy fluxes, because warm plumes ( $T' > 0$ ) rise due to buoyancy ( $w' > 0$ ). Above  $h = 1.5$  m the influence of surface-driven warm air advection decreases and the positive buoyancy fluxes are weaker which indicates the blending height. Above this height, flux differences can not be clearly attributed to the surface heterogeneities anymore but are already sufficiently mixed by the ambient flow. Close to the snow surface, we see an effect of the artificial topography on the buoyancy fluxes. On the downwind side of the local terrain height maxima, pronounced negative fluxes develop. The small regions just upwind of these maxima exhibit at least zero or slightly positive fluxes. These differences can be driven by warm air sweeps. When a wind gust advects warm air near the snow surface, the flow follows the local topography. On the upwind side of local terrain maxima  $w' > 0$  and  $T' > 0 \rightarrow w'T' > 0$ , while behind the maxima  $w' < 0$  and  $T' > 0 \rightarrow w'T' < 0$ . The maximum negative values of the buoyancy fluxes occur around the upper boundary of the cold air layer visible in Figures 4C, E. The cold air layer grows with low wind speeds until a wind gust replaces it with warmer air. These sweep events lead to pronounced negative buoyancy fluxes. Further downwind ( $x > 6$  m), the cold layer close to the surface is already deep enough that the sweeps cannot reach down to the surface anymore. Additionally, the air, initially heated up over bare ground, has already cooled down so that the temperature heterogeneities are not as pronounced as for smaller fetch distances over snow. The resulting increased energy input at the leading edge of the snow patch leads to accelerated melt described in previous experimental studies (Mott et al., 2011; Schlögl et al., 2018a).

The SIBL depth depicted in Figure 5B can be nicely described by the fit reviewed in Brutsaert (1982). At the very leading edge ( $x < 0.4$  m) the grid spacing in the LES simulation seems to be

too coarse to properly resolve the turbulent scales leading to the development of a shallow SIBL. However, the fit parameter (7), determining the growth rate does deviate from previously found values for step changes in surface roughness. Elliott (1958) and Bradley (1968) (as reviewed by Brutsaert (1982)) report typical values for neutral conditions of  $b = 0.7 - 0.8$ . More recently Granger et al. (2006) also investigated the SIBL growth adjacent to snow downwind of a transition from bare ground to snow. Depending on the roughness of the surface in the upwind direction, they found values of  $b = 0.5 - 0.62$  and  $c = 0.18 - 0.64$ , which are just larger than the values of our fitting parameters. However, Granger et al. (2006) compared air temperature upwind and downwind of the transition to diagnose the SIBL depth. They defined the upper SIBL boundary as the height above which both profiles overlap, which is higher than the depth of the (statically) stable layer. Consequently, we expect shallower SIBLs with our definition. In fact, Granger et al. (2006) report SIBL depths according to their best fits of  $h_{SIBL, Granger2006} \approx 0.3 \text{ m} - 0.9 \text{ m}$  at a fetch distance over snow of  $x = 2$  m, whereas our best-fit power law only yields a SIBL depth of  $h_{SIBL} = 0.18 \text{ m}$ . With the same temperature profile modification approach to estimate the SIBL depth, Takahara and Higuchi (1985) also suggest slightly deeper SIBLs.

#### 4.3 Near-surface boundary layer for low and high wind speeds

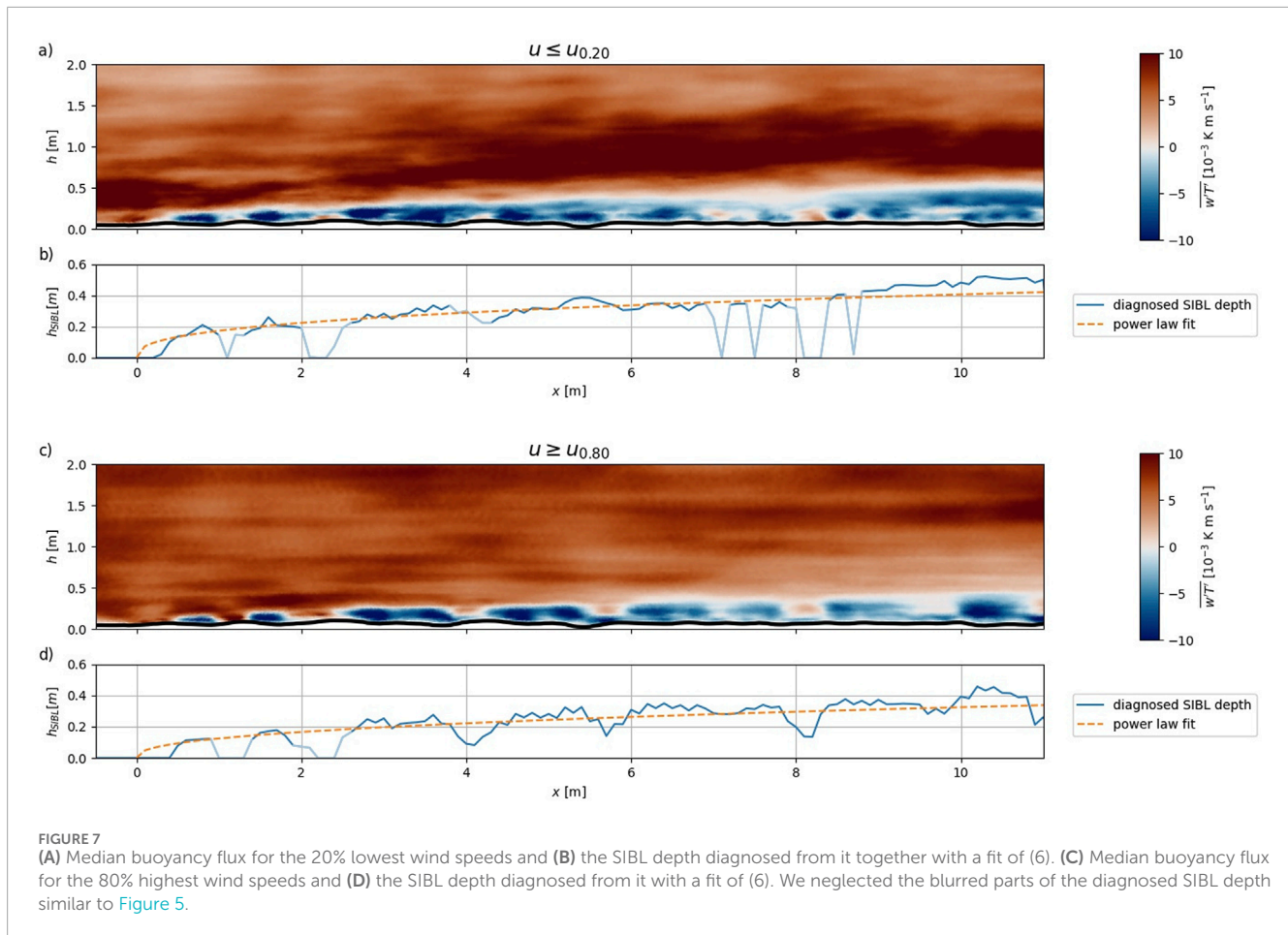
The results of the LES simulation are well suited to study not only the median flow properties but also the influence of the ambient wind speed on the near-surface boundary layer. In the following, we examine how the near-surface boundary layer changes during periods of low and high wind speeds. We therefore filter the data using the wind speed at  $x = 0$  m,  $y = 3.0$  m, and  $h = 1.5$  m after calculating all fluxes. The low wind speed class comprises periods with the 20% lowest wind speeds. ( $\leq 20\%$ -quantile). We denote this class by " $u \leq u_{0.2}$ ". On the contrary, the high wind speed class contains the 20% highest wind speeds ( $\geq 80\%$ -quantile). This



class is abbreviated by “ $u \geq u_{0.8}$ ”. Therefore, both classes contain the equivalent of 1 min data.

Figure 6 compares vertical profiles for both classes. The temperature profiles in Figures 6A, B show a growing depth of the statically stable layer close to the surface with fetch distance. Furthermore, a dependency of its depth on the wind speed is apparent. Higher wind speeds coincide with shallower statically stable layers. For example, the depth difference at  $x = 2\text{m}$  between the two wind speed classes is  $\Delta h_{ssl,x=2m} = 0.09\text{m}$  and at  $x = 10.5\text{m}$   $\Delta h_{ssl,x=10.5m} = 0.30\text{m}$ . During periods of low wind, a deeper

layer over snow can cool down. In contrast, the high wind speeds intermittently advect warm air from over bare ground limiting the depth of the statically stable layer. The buoyancy fluxes presented in Figures 6C, D support this observation. The layer of negative buoyancy fluxes in line with statically stable conditions close to the snow surface is deeper for low wind speeds. Furthermore, during calm periods the median and the 25%-quantile of the buoyancy fluxes, especially at the leading edge of the snow patch ( $x = 0.5\text{m}$  and  $x = 2\text{m}$ ) indicate slightly stronger negative fluxes. The energy from cooling the near-surface



air during calm periods is transferred to the snow surface. When the snow is already at 0°C, the additional energy is available for melt.

Layers of different stability also leave their footprints in the profiles of the horizontal wind speed shown in Figures 6E, F. During the quiescent periods the profile at  $x = 10.5$  m shows a kink at the upper boundary of the SIBL. With high wind speeds, the flow accelerates above the SIBL and forms a jet. The decoupled stable layer adjacent to the surface seems to act like a nozzle to the flow aloft. The effect is similar to the speed up of wind above ridge crests at larger scales such as demonstrated in Reynolds et al. (2023).

To further study the heat transfer, especially close to the surface, where reliable measurements are challenging, Figure 7 shows buoyancy fluxes and diagnosed SIBL depths for low and high wind speeds. The setup for each wind speed class is similar to Figure 5. In line with the discussion of the profiles above, we can directly see that the layer of negative fluxes adjacent to the snow surface, the SIBL, is deeper for low wind speeds. The power-law fit yields a SIBL depth at  $x = 10$  m of  $h_{SIBL, u \leq u_{0,20}} = 0.41$  m for low wind speeds and  $h_{SIBL, u \geq u_{0,80}} = 0.32$  m for high wind speeds. Shallower SIBLs with higher wind speeds are in contrast to the findings of Mott et al. (2013). Analyzing field data, they associate deep SIBLs with high wind speeds through enhanced generation of shear turbulence. Also, Granger et al. (2006) investigated the SIBL growth in dependency of the Weisman horizontal stability parameter (Weisman, 1977). Their Figure 8

indicates, that with increased shear, i.e., generated by higher wind speed, shallower SIBLs develop, which is in accordance with our findings.

We see from Figure 7 that the buoyancy fluxes within the SIBL are spatially heterogeneous. There are regions with pronounced negative buoyancy fluxes next to regions with positive fluxes. Especially during periods of high wind speeds (Figure 7D), sharp transitions between these regions of fluxes with opposite signs are apparent. This horizontal flux divergence seems to be driven by an interplay of the local wind field with the topography. It points to the fact that the SIBL, and the atmospheric layer adjacent to the snow patch generally, is spatio-temporally highly heterogeneous.

In order to also explore the influence of air temperature on the growth of the SIBL, we conducted further analysis. However, we found that near-surface air temperatures had negligible effects. We provide a figure showing the SIBL growth for low and high air temperatures (similar to Figure 7), along with a brief analysis, in the supplement.

## 5 Conclusions, limitations, and outlook

In the present study, we set up a centimeter-resolution large eddy simulation to model the near-surface atmospheric flow across

an idealized transition from bare ground to snow. We force the inflow-outflow model with high-frequency eddy covariance data recorded during a comprehensive field campaign in patchy snow conditions. Validation with independent high-frequency data shows that the model can reasonably reproduce horizontal wind speed and energy density spectra. However, the model lacks vertical motion and some high-frequency air temperature fluctuations as captured by the measurements. Sensitivity analysis indicates that this disparity may stem from the cell size. Within this highly heterogeneous setting, some energy-containing eddies appear smaller than the chosen horizontal grid spacing of 4 cm. We explain this for the following reasons: (1) artificially smoothed surface, (2) insufficient inflow description and (3) restriction of large-scale motions through the model domain dimensions. As our sensitivity analyses indicate, even state-of-the-art subgrid-scale models cannot adequately parameterize these effects on the centimeter scale. Vertical exchange is a crucial factor determining the structure of the near-surface atmosphere. The lack of representation by our model might lead to an underestimation of the SIBL depths and points to the need for improvements. However, we think that semi-quantitative analyses as presented above still offer valuable insights into the SIBL dynamics. Furthermore, the model adeptly reproduces flow features observed using measurements with a thermal infrared camera pointing at vertically deployed thin synthetic screens. It accurately depicts buoyant plumes of warm air intermittently detaching from the bare ground and being transported over the snow surface. This process is highly dynamic with time scales of only a few seconds. In addition, the simulation results enable us to investigate the growth of a thermal stable internal boundary layer (SIBL) adjacent to the snow surface. We show that the upper boundary of the SIBL can be well described by a power law as suggested by the literature. Moreover, by distinguishing quiescent periods from periods with higher wind speeds, we can show that the wind speed influences the growth of the SIBL. A slightly deeper SIBL can develop with low wind speeds, while higher wind speeds limit its growth. The results also show that the buoyancy fluxes are spatially heterogeneous and driven by terrain roughness even within the lowest layer adjacent to the surface.

Our simulations suggest two further research directions: First, using a finer grid could improve the representation of small-scale turbulence near the surface, especially vertical exchange. This could be achieved by nesting a smaller-domain DNS within the current LES setup to focus on the atmosphere adjacent to the surface. Second, extending the domain with a coarser grid is crucial for developing a physically grounded parameterization of atmospheric processes over highly heterogeneous surfaces. Incorporating actual snow cover distributions as a lower boundary condition helps to quantify the energy exchange between snow and atmosphere on a larger scale spanning tens to hundreds of meters. These scales align with those typically employed in state-of-the-art regional-scale numerical weather models, enabling direct comparisons between the two modeling estimates. The obtained results may be relevant not only for snow hydrological modeling but also for enhancing the performance of atmospheric models.

## Data availability statement

The datasets for this study can be found under <https://www.doi.org/10.16904/envidat.500>. The source code for the analysis presented in this study is accessible under [https://github.com/michhau/les\\_paper\\_24/tree/main](https://github.com/michhau/les_paper_24/tree/main).

## Author contributions

MH: Conceptualization, Data curation, Formal Analysis, Investigation, Methodology, Software, Validation, Visualization, Writing—original draft, Writing—review and editing. ML: Conceptualization, Funding acquisition, Methodology, Project administration, Supervision, Writing—review and editing. OH: Investigation, Methodology, Software, Writing—review and editing. MJ: Investigation, Methodology, Software, Writing—review and editing. DR: Investigation, Methodology, Writing—review and editing. RM: Conceptualization, Funding acquisition, Methodology, Project administration, Supervision, Writing—original draft, Writing—review and editing.

## Funding

The author(s) declare that financial support was received for the research, authorship, and/or publication of this article. This work is funded by the Swiss National Science Foundation (SNF) project “Snow–atmosphere interactions in mountains: Assessing wind-driven coupling processes and snow-albedo-temperature feedbacks” (nr. 188554). Open access funding by Swiss Federal Institute for Forest, Snow and Landscape Research (WSL).

## Acknowledgments

We thank the three anonymous reviewers for their valuable and constructive comments. Furthermore, our gratitude goes to Larissa Schädler for recording UAV orthophotos and assisting during the field campaign. Moreover, we acknowledge OpenAI ChatGPT that we used for language editing of the manuscript.

## Conflict of interest

The authors declare that the research was conducted in the absence of any commercial or financial relationships that could be construed as a potential conflict of interest.

The author(s) declared that they were an editorial board member of *Frontiers*, at the time of submission. This had no impact on the peer review process and the final decision.

## Publisher's note

All claims expressed in this article are solely those of the authors and do not necessarily represent those of their

affiliated organizations, or those of the publisher, the editors and the reviewers. Any product that may be evaluated in this article, or claim that may be made by its manufacturer, is not guaranteed or endorsed by the publisher.

## References

- Balogh, M., Parente, A., and Benocci, C. (2012). Rans simulation of abl flow over complex terrains applying an enhanced k- $\epsilon$  model and wall function formulation: implementation and comparison for fluent and openfoam. *J. Wind Eng. Industrial Aerodynamics* 104–106, 360–368. doi:10.1016/j.jweia.2012.02.023
- Bavay, M., Lehning, M., Jonas, T., and Löwe, H. (2009). Simulations of future snow cover and discharge in alpine headwater catchments. *Hydrol. Process.* 23, 95–108. doi:10.1002/hyp.7195
- Bradley, E. F. (1968). A micrometeorological study of velocity profiles and surface drag in the region modified by a change in surface roughness. *Q. J. R. Meteorological Soc.* 94, 361–379. doi:10.1002/qj.49709440111
- Brauchli, T., Trujillo, E., Huwald, H., and Lehning, M. (2017). Influence of slope-scale snowmelt on catchment response simulated with the *alpine3d* model. *Water Resour. Res.* 53, 10723–10739. doi:10.1002/2017WR021278
- Brutsaert, W. (1982). *Evaporation into the atmosphere*. Springer Netherlands. doi:10.1007/978-94-017-1497-6
- Carletti, F., Michel, A., Casale, F., Burri, A., Bocchiola, D., Bavay, M., et al. (2022). A comparison of hydrological models with different level of complexity in alpine regions in the context of climate change. *Hydrology Earth Syst. Sci.* 26, 3447–3475. doi:10.5194/hess-26-3447-2022
- Deardorff, J. W. (1974). Three-dimensional numerical study of the height and mean structure of a heated planetary boundary layer. *Boundary-Layer Meteorol.* 7, 81–106. doi:10.1007/BF00224974
- Elliott, W. P. (1958). The growth of the atmospheric internal boundary layer. *Eos, Trans. Am. Geophys. Union* 39, 1048–1054. doi:10.1029/TR039i006p1048
- Farina, S., and Zardi, D. (2023). Understanding thermally driven slope winds: recent advances and open questions. *Boundary-Layer Meteorol.* 189, 5–52. doi:10.1007/s10546-023-00821-1
- Föhn, P. M. B., and Meister, R. (1983). Distribution of snow drifts on ridge slopes: measurements and theoretical approximations. *Ann. Glaciol.* 4, 52–57. doi:10.3189/S0260305500005231
- Garratt, J. R. (1990). The internal boundary layer - a review. *Boundary-Layer Meteorol.* 50, 171–203. doi:10.1007/BF00120524
- Gerber, F., Mott, R., and Lehning, M. (2019). The importance of near-surface winter precipitation processes in complex alpine terrain. *J. Hydrometeorol.* 20, 177–196. doi:10.1175/JHM-D-18-0055.1
- Germano, M., Piomelli, U., Moin, P., and Cabot, W. H. (1991). A dynamic subgrid-scale eddy viscosity model. *Phys. Fluids A Fluid Dyn.* 3, 1760–1765. doi:10.1063/1.857955
- Granger, R. J., Essery, R., and Pomeroy, J. W. (2006). Boundary-layer growth over snow and soil patches: field observations. *Hydrol. Process.* 20, 943–951. doi:10.1002/hyp.6123
- Groffman, P. M., Driscoll, C. T., Fahey, T. J., Hardy, J. P., Fitzhugh, R. D., and Tierney, G. L. (2001). Colder soils in a warmer world: a snow manipulation study in a northern hardwood forest ecosystem. *Biogeochemistry* 56, 135–150. doi:10.1023/A:1013039830323
- Grudzielanek, A. M., and Cermak, J. (2015). Capturing cold-air flow using thermal imaging. *Boundary-Layer Meteorol.* 157, 321–332. doi:10.1007/s10546-015-0042-8
- Hames, O., Jafari, M., Wagner, D. N., Raphael, I., Clemens-Sewall, D., Polashenski, C., et al. (2022). Modeling the small-scale deposition of snow onto structured arctic sea ice during a mosaic storm using snowbedfoam 1.0. *Geosci. Model Dev.* 15, 6429–6449. doi:10.5194/gmd-15-6429-2022
- Harder, P., Pomeroy, J. W., and Helgason, W. (2017). Local-scale advection of sensible and latent heat during snowmelt. *Geophys. Res. Lett.* 44, 9769–9777. doi:10.1002/2017GL074394
- Haugeneder, M., Lehning, M., Reynolds, D., Jonas, T., and Mott, R. (2023). A novel method to quantify near-surface boundary-layer dynamics at ultra-high spatio-temporal resolution. *Boundary-Layer Meteorol.* 186, 177–197. doi:10.1007/s10546-022-00752-3
- Haugeneder, M., Lehning, M., Stiperski, I., Reynolds, D., and Mott, R. (2024). Turbulence in the strongly heterogeneous near-surface boundary layer over patchy snow. *Boundary-Layer Meteorol.* 190, 7. doi:10.1007/s10546-023-00856-4
- Högström, U. (1996). Review of some basic characteristics of the atmospheric surface layer. *Boundary-Layer Meteorol.* 78, 215–246. doi:10.1007/BF00120937
- Huang, J., and Bou-Zeid, E. (2013). Turbulence and vertical fluxes in the stable atmospheric boundary layer. part i: a large-eddy simulation study. *J. Atmos. Sci.* 70, 1513–1527. doi:10.1175/JAS-D-12-0167.1
- Jafari, M., Sharma, V., and Lehning, M. (2022). Convection of water vapour in snowpacks. *J. Fluid Mech.* 934, A38. doi:10.1017/jfm.2021.1146
- Johnson, R. H., Young, G. S., Toth, J. J., and Zehr, R. M. (1984). Mesoscale weather effects of variable snow cover over northeast Colorado. *Mon. Weather Rev.* 112, 1141–1152. doi:10.1175/1520-0493(1984)112<1141:mweovs>2.0.co;2
- Kljun, N., Calanca, P., Rotach, M. W., and Schmid, H. P. (2015). A simple two-dimensional parameterisation for flux footprint prediction (ffp). *Geosci. Model Dev.* 8, 3695–3713. doi:10.5194/gmd-8-3695-2015
- Kolmogorov, A. N. (1941). The local structure of turbulence in incompressible viscous fluid for very large Reynolds numbers. *Dokl. Akad. Nauk. SSSR* 30, 301–304.
- Lehning, M., Löwe, H., Ryser, M., and Raderschall, N. (2008). Inhomogeneous precipitation distribution and snow transport in steep terrain. *Water Resour. Res.* 44. doi:10.1029/2007WR006545
- Lehning, M., Völksch, I., Gustafsson, D., Nguyen, T. A., Stähli, M., and Zappa, M. (2006). *Alpine3d*: a detailed model of mountain surface processes and its application to snow hydrology. *Hydrol. Process.* 20, 2111–2128. doi:10.1002/hyp.6204
- Leslie, D. C., and Quarini, G. L. (1979). The application of turbulence theory to the formulation of subgrid modelling procedures. *J. Fluid Mech.* 91, 65. doi:10.1017/S0022112079000045
- Letcher, T. W., and Minder, J. R. (2017). The simulated response of diurnal mountain winds to regionally enhanced warming caused by the snow albedo feedback. *J. Atmos. Sci.* 74, 49–67. doi:10.1175/JAS-D-16-0158.1
- Li, D., Lettenmaier, D. P., Margulis, S. A., and Andreadis, K. (2019). The role of rain-on-snow in flooding over the conterminous United States. *Water Resour. Res.* 55, 8492–8513. doi:10.1029/2019WR024950
- Lund, T. (2003). The use of explicit filters in large eddy simulation. *Comput. & Math. Appl.* 46, 603–616. doi:10.1016/S0898-1221(03)90019-8
- Magnusson, J., Nævdal, G., Matt, F., Burkhart, J. F., and Winstral, A. (2020). Improving hydropower inflow forecasts by assimilating snow data. *Hydrology Res.* 51, 226–237. doi:10.2166/nh.2020.025
- Melo, D. B., Sigmund, A., and Lehning, M. (2024). Understanding snow saltation parameterizations: lessons from theory, experiments and numerical simulations. *Cryosphere* 18, 1287–1313. doi:10.5194/tc-18-1287-2024
- Ménard, C. B., Essery, R., and Pomeroy, J. (2014). Modelled sensitivity of the snow regime to topography, shrub fraction and shrub height. *Hydrology Earth Syst. Sci.* 18, 2375–2392. doi:10.5194/hess-18-2375-2014
- Meneveau, C., Lund, T. S., and Cabot, W. H. (1996). A Lagrangian dynamic subgrid-scale model of turbulence. *J. Fluid Mech.* 319, 353. doi:10.1017/S0022112096007379
- Mott, R., Daniels, M., and Lehning, M. (2015). Atmospheric flow development and associated changes in turbulent sensible heat flux over a patchy mountain snow cover. *J. Hydrometeorol.* 16, 1315–1340. doi:10.1175/JHM-D-14-0036.1
- Mott, R., Egli, L., Grünewald, T., Dawes, N., Manes, C., Bavay, M., et al. (2011). Micrometeorological processes driving snow ablation in an alpine catchment. *Cryosphere* 5, 1083–1098. doi:10.5194/tc-5-1083-2011
- Mott, R., Gromke, C., Grünewald, T., and Lehning, M. (2013). Relative importance of advective heat transport and boundary layer decoupling in the melt dynamics of a patchy snow cover. *Adv. Water Resour.* 55, 88–97. doi:10.1016/j.advwatres.2012.03.001
- Mott, R., Schlögl, S., Dirks, L., and Lehning, M. (2017). Impact of extreme land surface heterogeneity on micrometeorology over spring snow cover. *J. Hydrometeorol.* 18, 2705–2722. doi:10.1175/JHM-D-17-0074.1
- Mott, R., Winstral, A., Cluzet, B., Helbig, N., Magnusson, J., Mazzotti, G., et al. (2023). Operational snow-hydrological modeling for Switzerland. *Front. Earth Sci.* 11. doi:10.3389/feart.2023.1228158
- Moukalled, F., Mangani, L., and Darwish, M. (2016). *The finite volume method in computational fluid dynamics*, 113. Springer International Publishing. doi:10.1007/978-3-319-16874-6

## Supplementary material

The Supplementary Material for this article can be found online at: <https://www.frontiersin.org/articles/10.3389/feart.2024.1415327/full#supplementary-material>

- OpenFoam API Guide (2024). buoyantboussinesqpimplefoam.c file reference. Available at: [https://www.openfoam.com/documentation/guides/latest/api/buoyantBoussinesqPimpleFoam\\_8C.html](https://www.openfoam.com/documentation/guides/latest/api/buoyantBoussinesqPimpleFoam_8C.html) (Accessed April 3, 2024).
- Poletto, R., Craft, T., and Revell, A. (2013). A new divergence free synthetic eddy method for the reproduction of inlet flow conditions for les. *Flow, Turbul. Combust.* 91, 519–539. doi:10.1007/s10494-013-9488-2
- Pomeroy, J., and Gray, D. (1995). Snowcover accumulation, relocation and management NHRI science report No. *Natl. Hydrology Res. Inst.*
- Pope, S. B. (2000). *Turbulent flows*. Cambridge University Press. doi:10.1017/CBO9780511840531
- Quéno, L., Mott, R., Morin, P., Cluzet, B., Mazzotti, G., and Jonas, T. (2023). Snow redistribution in an intermediate-complexity snow hydrology modelling framework. *EGUsphere* 2023, 1–32. doi:10.5194/egusphere-2023-2071
- Reynolds, D., Gutmann, E., Kruyt, B., Haugeneder, M., Jonas, T., Gerber, F., et al. (2023). The high-resolution intermediate complexity atmospheric research (hicar v1.1) model enables fast dynamic downscaling to the hectometer scale. *Geosci. Model Dev.* 16, 5049–5068. doi:10.5194/gmd-16-5049-2023
- Reynolds, D., Quéno, L., Lehning, M., Jafari, M., Berg, J., Jonas, T., et al. (2024). Seasonal snow-atmosphere modeling: let's do it. *EGUsphere* 2024, 1–28. doi:10.5194/egusphere-2024-489
- Richardson, H., Basu, S., and Holtslag, A. A. M. (2013). Improving stable boundary-layer height estimation using a stability-dependent critical bulk richardson number. *Boundary-Layer Meteorol.* 148, 93–109. doi:10.1007/s10546-013-9812-3
- Rixen, C., Høye, T. T., Macek, P., Aerts, R., Alatalo, J. M., Anderson, J. T., et al. (2022). Winters are changing: snow effects on arctic and alpine tundra ecosystems. *Arct. Sci.* 8, 572–608. doi:10.1139/as-2020-0058
- Schlögl, S., Lehning, M., Fierz, C., and Mott, R. (2018a). Representation of horizontal transport processes in snowmelt modeling by applying a footprint approach. *Front. Earth Sci.* 6. doi:10.3389/feart.2018.00120
- Schlögl, S., Lehning, M., and Mott, R. (2018b). How are turbulent sensible heat fluxes and snow melt rates affected by a changing snow cover fraction? *Front. Earth Sci.* 6. doi:10.3389/feart.2018.00154
- Schotanus, P., Nieuwstadt, F., and Bruin, H. D. (1983). Temperature measurement with a sonic anemometer and its application to heat and moisture fluxes. *Boundary-Layer Meteorol.* 26, 81–93. doi:10.1007/BF00164332
- Sigmund, A., Dujardin, J., Comola, F., Sharma, V., Huwald, H., Melo, D. B., et al. (2022). Evidence of strong flux underestimation by bulk parametrizations during drifting and blowing snow. *Boundary-Layer Meteorol.* 182, 119–146. doi:10.1007/s10546-021-00653-x
- Siirila-Woodburn, E. R., Rhoades, A. M., Hatchett, B. J., Huning, L. S., Szinai, J., Tague, C., et al. (2021). A low-to-no snow future and its impacts on water resources in the western United States. *Nat. Rev. Earth & Environ.* 2, 800–819. doi:10.1038/s43017-021-00219-y
- Smagorinski, J. (1963). General circulation experiments with the primitive equations. *Mon. Weather Rev.* 91, 99–164. doi:10.1175/1520-0493(1963)091<0099:gcewtp>2.3.co;2
- Smith, C. M., and Porté-Agel, F. (2014). An intercomparison of subgrid models for large-eddy simulation of katabatic flows. *Q. J. R. Meteorological Soc.* 140, 1294–1303. doi:10.1002/qj.2212
- Stiperski, I., and Rotach, M. W. (2016). On the measurement of turbulence over complex mountainous terrain. *Boundary-Layer Meteorol.* 159, 97–121. doi:10.1007/s10546-015-0103-z
- Stoll, R., Gibbs, J. A., Salesky, S. T., Anderson, W., and Calaf, M. (2020). Large-eddy simulation of the atmospheric boundary layer. *Boundary-Layer Meteorol.* 177, 541–581. doi:10.1007/s10546-020-00556-3
- Stucchi, L., Bombelli, G., Bianchi, A., and Bocchiola, D. (2019). Hydropower from the alpine cryosphere in the era of climate change: the case of the sabbione storage plant in Italy. *Water* 11, 1599. doi:10.3390/w11081599
- Stull, R. B. (1988). *An introduction to boundary layer meteorology*. Springer Netherlands. doi:10.1007/978-94-009-3027-8
- Sturm, M., Goldstein, M. A., and Parr, C. (2017). Water and life from snow: a trillion dollar science question. *Water Resour. Res.* 53, 3534–3544. doi:10.1002/2017WR020840
- Sui, J., and Koehler, G. (2001). Rain-on-snow induced flood events in southern Germany. *J. Hydrology* 252, 205–220. doi:10.1016/S0022-1694(01)00460-7
- Takahara, H., and Higuchi, K. (1985). Thermal modification of air moving over melting snow surfaces. *Ann. Glaciol.* 6, 235–237. doi:10.3189/1985AoG6-1-235-237
- Urfer-Henneberger, C. (1970). Neuere beobachtungen über die entwicklung des schönwetterwindsystems in einem v-förmigen alpental (dischmatal bei davos). *Arch. für Meteorol. Geophys. Bioklimatol. Ser. B* 18, 21–42. doi:10.1007/BF02245866
- van der Valk, L. D., Teuling, A. J., Girod, L., Pirk, N., Stoffer, R., and van Heerwaarden, C. C. (2022). Understanding wind-driven melt of patchy snow cover. *Cryosphere* 16, 4319–4341. doi:10.5194/tc-16-4319-2022
- Weisman, R. N. (1977). Snowmelt: a two-dimensional turbulent diffusion model. *Water Resour. Res.* 13, 337–342. doi:10.1029/WR013i002p00337
- Weller, H. G., Tabor, G., Jasak, H., and Fureby, C. (1998). A tensorial approach to computational continuum mechanics using object-oriented techniques. *Comput. Phys.* 12, 620–631. doi:10.1063/1.168744
- Wever, N., Comola, F., Bavay, M., and Lehning, M. (2017). Simulating the influence of snow surface processes on soil moisture dynamics and streamflow generation in an alpine catchment. *Hydrology Earth Syst. Sci.* 21, 4053–4071. doi:10.5194/hess-21-4053-2017
- Wheeler, J. A., Cortés, A. J., Sedlacek, J., Karrenberg, S., van Kleunen, M., Wipf, S., et al. (2016). The snow and the willows: earlier spring snowmelt reduces performance in the low-lying alpine shrub *Salix herbacea*. *J. Ecol.* 104, 1041–1050. doi:10.1111/1365-2745.12579
- Wipf, S., and Rixen, C. (2010). A review of snow manipulation experiments in arctic and alpine tundra ecosystems. *Polar Res.* 29, 95–109. doi:10.1111/j.1519-8369.2010.00153.x
- Würzer, S., Jonas, T., Wever, N., and Lehning, M. (2016). Influence of initial snowpack properties on runoff formation during rain-on-snow events. *J. Hydrometeorol.* 17, 1801–1815. doi:10.1175/JHM-D-15-0181.1
- Zahn, E., and Bou-Zeid, E. (2024). Setting up a large-eddy simulation to focus on the atmospheric surface layer. *Boundary-Layer Meteorol.* 190, 12. doi:10.1007/s10546-023-00841-x
- Zwaafink, C. D. G., Diebold, M., Horender, S., Overney, J., Lieberherr, G., Parlange, M. B., et al. (2014). Modelling small-scale drifting snow with a Lagrangian stochastic model based on large-eddy simulations. *Boundary-Layer Meteorol.* 153, 117–139. doi:10.1007/s10546-014-9934-2